ACS NANO

www.acsnano.org

ARTICLE

Size-Resolved Shape Evolution in Inorganic Nanocrystals Captured via High-Throughput Deep Learning-Driven Statistical Characterization

Min Gee Cho,* Katherine Sytwu, Luis Rangel DaCosta, Catherine Groschner, Myoung Hwan Oh, and Mary C. Scott*

Cite This: *ACS Nano* 2024, 18, 29736–29747

Read Online

ACCESS | Metrics & More | Article Recommendations | Supporting Information

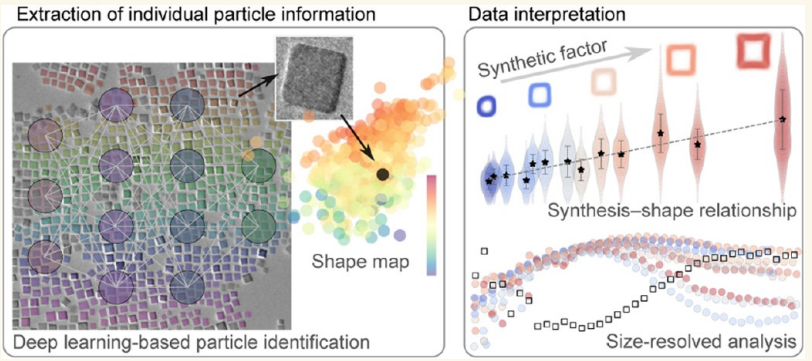

ABSTRACT: Precise size and shape control in nanocrystal synthesis is essential for utilizing nanocrystals in various industrial applications, such as catalysis, sensing, and energy conversion. However, traditional ensemble measurements often overlook the subtle size and shape distributions of individual nanocrystals, hindering the establishment of robust structure−property relationships. In this study, we uncover intricate shape evolutions and growth mechanisms in Co_3O_4 nanocrystal synthesis at a subnanometer scale, enabled by deep-learning-assisted statistical characterization. By first controlling synthetic parameters such as cobalt precursor concentration and water amount then using high resolution electron microscopy imaging to identify the geometric features of individual nanocrystals, this study provides insights into the interplay between synthesis conditions and the size-dependent shape evolution in colloidal nanocrystals. Utilizing population-wide imaging data encompassing over 441,067 nanocrystals, we analyze their characteristics and elucidate previously unobserved size-resolved shape evolution. This high-throughput statistical analysis is essential for representing the entire population accurately and enables the study of the size dependency of growth regimes in shaping nanocrystals. Our findings provide experimental quantification of the growth regime transition based on the size of the crystals, specifically (i) for faceting and (ii) from thermodynamic to kinetic, as evidenced by transitions from convex to concave polyhedral crystals. Additionally, we introduce the concept of an "onset radius," which describes the critical size thresholds at which these transitions occur. This discovery has implications beyond achieving nanocrystals with desired morphology; it enables finely tuned correlation between geometry and material properties, advancing the field of colloidal nanocrystal synthesis and its applications.

continued...

Received: July 11, 2024
Revised: October 2, 2024
Accepted: October 8, 2024
Published: October 19, 2024

https://doi.org/10.1021/acsnano.4c09312
ACS Nano 2024, 18, 29736−29747

KEYWORDS: *nanocrystal synthesis, high-resolution TEM, deep learning, image analysis, high-throughput statistical analysis, size-resolved analysis, growth regimes*

INTRODUCTION

Over the last few decades, significant strides have been made in precisely controlling the size and shape of inorganic nanocrystals, progress further accelerated by the discovery and synthesis of quantum dots with size-dependent properties.[1−6] Altering the size and shape of nanocrystals is of interest since it directly influences their exposed surface facets, impacting their surface energy, which plays a key role in various surface reactions.[7−10] Mechanistic studies of nanocrystal shaping have been conducted by systematically controlling synthetic conditions, such as varying the type and concentration of metal precursors and capping agents, to examine the role of thermodynamic and kinetic parameters. Traditionally, "monodisperse" nanocrystals are described as having uniform size and shape, but their shapes have often been observed qualitatively without precise quantification of their distribution. However, achieving true monodispersity critically depends on accurate size and shape measurements. If the distribution fails to represent the entire population, the derived relationships between size, shape, and synthetic parameters remain uncertain. Furthermore, the shape of nanocrystals can vary depending on their size, and shape variance among nanocrystals might exist within the same sample. This variability complicates the accurate assessment of their uniformity and can lead to misinterpretation of their properties and behavior when based on small data sets.

Commonly used nanocrystal size measurements rely on ensemble techniques, such as applying the Sherrer equation to X-ray diffraction data. Although X-ray techniques are suitable for obtaining the bulk information due to their deep probing depth, they generally offer lower spatial resolution and are less effective for surface morphology studies. This limitation prevents precise distribution measurements for individual nanocrystals, thereby complicating the structure−property relationship and placing additional constraints on the design and synthesis of nanocrystals with desired functionalities. In contrast, electron microscopy measures individual nanoparticles with high-resolution capabilities, capturing detailed structural information at the nanoscale. While electron microscopy images enable detailed high-resolution analysis, the manual analysis of images is limited in throughput. The absence of precise, high-throughput measurements on individual nanocrystals to obtain size and shape distributions, especially the shape, has limited not only control over the overall morphology of nanocrystals but also the establishment of relationships between nanocrystal sizes, shapes and their properties.

Computer vision and advanced machine learning techniques, such as neural networks, can bridge the gap between colloidal synthesis and statistical analysis by processing extensive data sets containing characteristics from individual particles.[11−18] Recent advancements in statistical image analyses offer a robust approach by measuring the size and shape of a significant number of distinct particles to represent the entire nanocrystal population.[19−22] However, the techniques developed so far have primarily focused on relatively large nanoparticles, mostly larger than several tens of nanometers, where in most cases, do not need a subnanometer scale accuracy in measurements. In contrast, analyzing smaller nanoparticles requires high-magnification imaging, which introduces additional image features. High-resolution transmission electron microscopy (TEM) images not only differ in pixel size but also exhibit increased textural complexity, such as lattice fringes, making traditional segmentation methods less effective. These finer details, along with lower amplitude and phase contrast, as well as a reduced signal-to-noise ratio, necessitate more advanced segmentation techniques to accurately resolve surface features.

We use high-throughput, deep learning-assisted computer vision to identify and measure geometric features of individual nanocrystals with sizes less than 10 nm, enabling a detailed statistical analysis of size and shape distributions that allows us to study shape variations and correlate shape with size at a subnanometer level. Our approach provides a more comprehensive understanding of nanocrystal morphology with high precision, highlighting variations and subtleties that are not apparent through traditional qualitative analysis alone. Moreover, size-resolved observations, which were previously unavailable due to the lack of measurement tools and insufficient data size in prior research, are now possible with our technique. We validated our approach through a population-wide study of cuboid Co_3O_4,[23] given their significant interest due to high electrocatalytic properties in the oxygen evolution reaction and $Li−O_2$ batteries.[9,10,24−27] We analyze 441,067 individual nanocrystals from various sol−gel synthesis conditions, enabled by a convolutional neural network (CNN) for computer vision to solve complex segmentation challenges in high-resolution transmission electron microscopy (HRTEM) images. Trained neural networks efficiently detect individual nanocrystals, enabling further analysis in the size-resolved shape variations in nanocrystal samples.

With our approach, we achieved two noteworthy breakthroughs in nanoscience. First, even when dealing with polydisperse nanocrystals, our detailed statistical analysis offers refined guidance for synthesizing nanocrystals with specific size and shape attributes. By precisely correlating synthetic variables, such as cobalt precursor concentration and water amount, with nanocrystal size and shape, we can optimize synthesis conditions to achieve desired properties more accurately than traditional methods. Second, we experimentally discovered the "onset radius" for the transitions: (i) from spherical to Wulff shape and (ii) from thermodynamic- to kinetic-controlled growth mode, enabled by precise and semiautomated high-throughput shape measurements. Our study extends beyond the development of CNNs for precise segmentation in high-resolution electron micrographs and demonstrates how they can be applied to reveal the role of synthetic parameters and critical size thresholds in growth regimes.

RESULTS AND DISCUSSION

Workflow for High-Throughput Statistical Characterization of Nanocrystals. The overall workflow begins with the colloidal synthesis of inorganic nanocrystals, followed by high-resolution imaging of the nanocrystals using a transmission electron microscope (TEM), training a neural network to segment the TEM images, and conducting statistical analysis on the distribution of nanocrystals in terms of size and various shape descriptors (Figure 1). We chose spinel Co_3O_4 polyhedral nanocrystals to validate the platform's capabilities. Precise

https://doi.org/10.1021/acsnano.4c09312
ACS Nano 2024, 18, 29736−29747

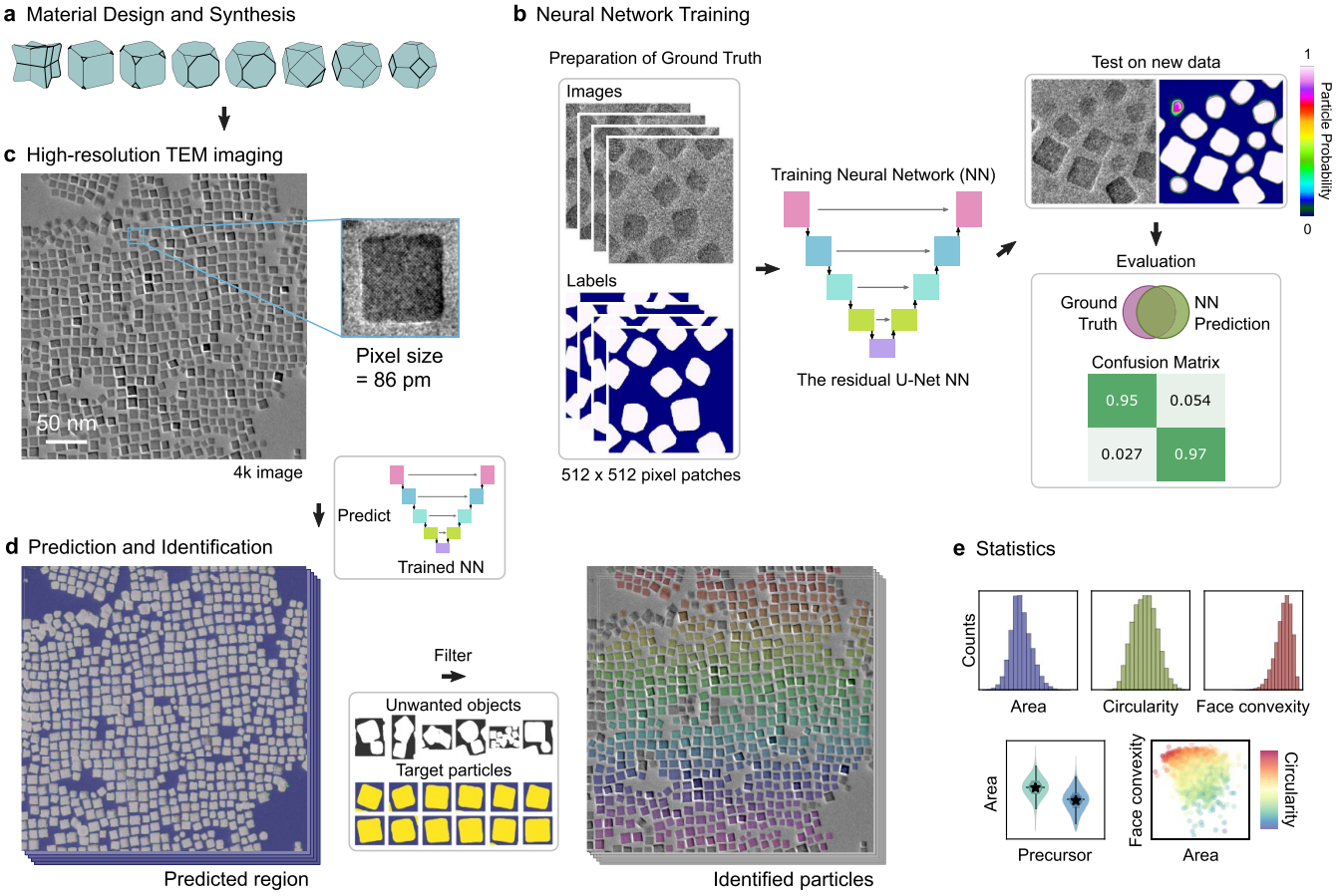

Figure 1. Overview of the workflow from nanocrystal synthesis to statistical analysis. a, Illustrations of the diversity of as-synthesized cobalt oxide nanocrystals, showcasing variations in size and shape, including truncated cubes, truncated octahedrons, and cubes with concave surfaces. b, Overview of the CNN training, testing, and evaluation process. The architecture of an 18-layer deep residual U-Net is used for model training. Training data sets are prepared through manual labeling of images, and the trained neural network predicts particle regions in new TEM images, and its performance is evaluated using the F1-score. The confusion matrix in (b) shows an example of soft Dice scores for neural network performance. c, Example of a HRTEM image captured using an aberration-corrected microscope at a resolution of 4k (4096 × 4096). Pixel size is 86 pm. d, e, Prediction (d) and statistical characterization (e) of individual particles in 4k images by the trained neural network, alongside the identification of individual particles. A filter is applied to exclude overlapping, irregularly shaped, and poorly segmented particles. Particles that pass the filter are then analyzed through various data visualizations.

control over the synthesis conditions allows us to achieve desired sizes and shapes of the nanocrystals, optimizing their properties for specific applications. Using our synthetic procedure based on colloidal systems, which we slightly modified from a previous report,[23] we synthesize sub-10 nm cuboid Co_3O_4 nanocrystals. These nanocrystals are dominantly enclosed with {100} facets and exhibit slight truncation at the edges and/or corners. This process enables us to produce nanocrystals under different experimental conditions to achieve the desired geometrical characteristics (Figure 1a and Figure S1).

Leveraging our deep learning-based platform, we identified the size, shape, and monodispersity of several hundred thousand Co_3O_4 nanocrystals at the subnanometer scale. The high-throughput analysis of 727 electron microscopy images of 441,067 nanocrystals was enabled by a convolutional neural network with a residual U-Net architecture (Figure 1b and Table S1).[16,28,29] This U-Net architecture is an effective way to achieve high performance in segmenting, or pixel-wise classification, between particle and background regions.[16,17,30] To distinguish the variations in the structural features at a subnanometer level with high precision, we acquired high-resolution 4k (4096 × 4096 pixel) TEM images with a pixel size of 86 pm (Figure 1c). To train the neural network, raw images were selected from the larger data set and labeled by hand into segmented images using Image Labeler, a Matlab application (see Methods for details). The data set, comprising pairs of images and labels (ground truth), were then split into 512 × 512 pixel patches to minimize GPU memory requirements and fed into the deep learning model (Figure 1b). The networks were trained using both cross-entropy and Dice loss functions, softmax activation function, and the Adam optimizer with a decaying learning rate, facilitating the model to converge at the optimal score and loss values and get the final model with the least loss. To evaluate the neural network's ability to segment nanocrystals in the images, we used the Dice coefficient, also known as the F1-score (Figure S2). The Dice coefficient, a standard metric for segmentation tasks, quantifies the normalized union of positive pixels between true and predicted segmentation labels and is visualized in a confusion-matrix style (Figure 1c). To enable generalization across various nanocrystal samples and imaging sessions, we preprocessed the images, including flat-field correction and rescaling of image values (standardization).[30]

https://doi.org/10.1021/acsnano.4c09312
ACS Nano 2024, 18, 29736−29747

The trained neural net predicts particle regions in preprocessed full-resolution 4k images and the binary-classified particle pixels are identified as individual particle regions using the scikit-image package, a Python image processing tool (Figure 1d). Size and shape statistics of the segmented particle regions are then analyzed using geometric shape descriptors (Figure 1e). To quantitatively analyze the morphological evolution both between and within samples prepared under various synthetic conditions, we compared the geometric features of the nanocrystals using three simple shape descriptors: edge length (nm; $\sqrt{\text{area}}$), circularity ($4\pi \times$ object area/object perimeter^2), and face convexity (object area/convex hull area) (Figure S2).[13] To find and filter out unwanted objects such as overlapping particles and particle agglomerates from downstream analysis, we use two convexity measurements (i.e., line- and area-based convexity) to identify these mostly nonconvex objects (Figure S3). The area-based convexity is referred to as "face convexity" in this study due to the absence of a hollow portion within the nanocrystal.

Empirical Analysis of Data Size Requirements for Reliable Statistical Characterization. High-throughput imaging with HRTEM often introduces inherent sampling biases due to uneven nanoparticle distribution on the grid. To mitigate these biases and determine the data size required for reliable statistical analysis, we performed an empirical comparison by grouping the data. By dividing the 65,000-particle data set from 78 images of a single synthesis condition (the 'Co0.4' sample) into several groups, we systematically compared the statistics of each group with the same data size to understand how sample size affects the statistical results. Figure 2 illustrates the comparison of statistical results using two different grouping methods—sequential (Figure 2a–c) and random (Figure 2d,e). As shown in Figure 2a, when sequentially grouping the data, where particles are assigned to groups based on their image acquisition order, the difference in mean values of edge length between groups decreases with increasing sample size. For example, when grouping the data into three different groups and comparing the first 1000 particles in each group, the mean values differ greatly depending on the group (Figure 2a). This is potentially due to the possibility that when groups are divided by sequentially extracting particles from TEM images, the assembly of particles in nearby locations can be similar in size, which may affect the statistical results (see Table S1 for the number of particles and images analyzed for each sample). For this reason, to include the diversity of nanocrystal characteristics that covers the entire population, a larger data size is needed. As the data size of subgroups increases to 3000, 5000, and 10,000, the differences between groups become smaller, and the statistical distribution becomes more similar to that of the whole group, indicating that the group represents the entire population well (Figure 2b and Figure S4). For a more robust comparison and exploration of statistical results across different data sizes, we analyzed the necessary group size needed to obtain reliable statistical results over 65,000 particles (e.g., divided into 65, 10, and 3 groups of 1000, 6000, and 20,000 particles each, respectively) (Figure 2c) (see Figure S5 for grouping based on the number of images). When the number of particles exceeds 5000, the coefficient of variance (CV) of mean values between groups is around 4% and decreases to around 2% at a data size of 10,000. We examined and compared the CV values of various nanocrystal samples, finding that regardless of the sample, when the data size reaches 5000, the CV is reduced to half its value compared to a data size of 500 (Figure S5). Additionally,

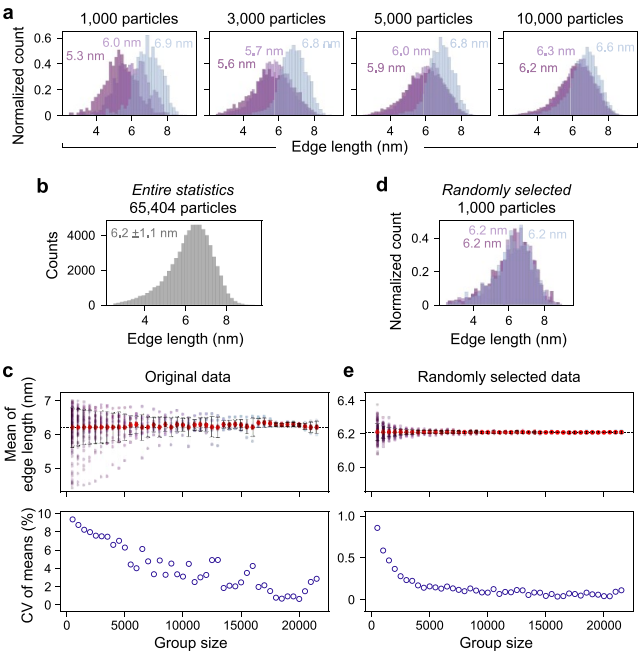

Figure 2. Effect of data size on statistical results. a, Histograms showing a comparison of statistical analysis methods by evaluating the mean of edge length values in each group, where each group represents data of the same size but with different particles. b, Histogram of entire statistics including 65,404 particles. c, Mean edge length values among different group sizes of data sequentially selected by naively counting nanoparticles in consecutive images. d, A randomly selected subset of 1000 particles out of the total 65,404 particles effectively represents the statistical distribution. e, Mean edge length values among different group sizes of randomly selected data. The dotted horizontal lines in (c) and (e) represents the global mean values of the edge length. Navy circles denote the CV values between the mean values of each group. A higher CV value indicates a greater disparity in mean values between groups within that data size, which means significantly different statistical outcomes depending on the choice of groups.

although the extent of CV reduction varies by sample, in all cases, the CV either remains the same or decreases further after the data size reaches 5000. Based on these observations, we decided to obtain data for more than 20,000 particles per sample to ensure reliable statistical results (see Table S1).

The statistical distributions of the shape properties of the particles are then visualized in histograms, violin plots, scatter plots, and contour plots (Figure 1e). Multiple visualizations are essential to capture the different aspects of the data comprehensively. While histograms encompass all measured features of objects and provide a clear view of the frequency distribution of the shape properties, they still represent a form of data reduction. Using scatter plots, not only can individual information be preserved, but they also allow us to understand correlations between variables. However, large data sets necessary to reflect information from an entire population pose challenges in effectively discerning distribution information at the individual level, due to redundancy, overlapping data points, and reduced visual clarity. To address this visualization issue, we generated a reduced data set by selecting a specific number of particles from each nanocrystal sample. To mitigate the sequential acquisition bias seen in Figure 2c, we adopted a random selection method by shuffling particle data and subsequently selecting the reduced number of particles. With

https://doi.org/10.1021/acsnano.4c09312
ACS Nano 2024, 18, 29736–29747

random sampling, a smaller data set can accurately represent the larger population. For example, 1000 particles were randomly chosen three times and each group appears to have substantially similar mean values (Figure 2d). Their distribution shapes are already similar to that of the whole group with only a relatively small data size of 1000. Figure 2e shows the trend in the mean value difference between groups depending on the group size. Notably, a data size of 2000 can effectively capture population characteristics when selected uniformly at random from the entire population, and even a data size of 1000 shows a low CV of about 1%, indicating its suitability for analysis with a reduced data size. Note that this approach still requires collecting a large data set, as it is currently impractical to experimentally randomly sample individual nanoparticles. This high-throughput sampling ensures that even with a smaller data size used during analysis, we achieve robust and reliable statistical insights.

Effect of Cobalt Precursor and Water on Nanocrystal Geometry. Recent strategies for the synthesis of spinel oxide nanocrystals are based on the use of an alcohol/water system, employing the organic/aqueous interface of reverse vesicles as the reaction medium.[23,31−34] In our study, Co_3O_4 nanocrystals were synthesized in the reaction medium of cobalt(II) perchlorate precursors, 1-octanol, oleylamine, and water (Methods). Cobalt precursors and water play crucial roles throughout the entire synthesis process, including the conversion of metal precursors into monomers—the fundamental building units of the nanocrystals—and the subsequent growth phase. During the reaction, hydrated $Co(ClO_4)_2$ precursor complexes with 1-octanol and oleylamine to form a cobalt−ligand complex. The complex acts as a premonomeric species that will be converted to monomers.[35,36] The hydrolysis of the metal−ligand complex in the solution is accelerated by the injection of water, leading to the formation of monomers, which can further condense to form metal−oxygen−metal bridges.[37] The concentration of cobalt precursors influences the proportion of 1-octanol ligands per cobalt ion center, affecting the number of binding sites and, consequently, the supersaturation level of monomers. Higher concentrations of cobalt precursors result in fewer 1-octanol ligands per cobalt ion center, reducing the binding sites for oleylamine ligands at a given oleylamine amount, which in turn lowers the monomer supersaturation level. Conversely, more water in the solution increases the supersaturation level by converting more cobalt−ligand complexes into water ligands. In our study, the reaction temperature (120 °C), reaction time, and the type and amount of ligands (oleylamine and 1-octanol) are kept constant to isolate the effect of the initial cobalt concentration and water amount. Therefore, to control the size and shape of the nanocrystals, we varied the synthetic parameters such as cobalt precursor amount (0.2 to 0.8 mmol) and water amount (0.43 to 1.0 mL).

The representative images and shape statistics of the samples produced with varying amounts of cobalt precursor and water are shown in Figures 3 and 4, respectively. The synthesis conducted at lower cobalt concentrations yielded small, round, and mostly convex nanocrystals, as shown in the TEM images (Figure 3; Co0.2−Co0.8). This trend is also apparent in the histograms; with higher initial cobalt precursor concentrations, the mean edge length increases while circularity and face convexity decrease. For reference, a circle has a circularity of 1, while a square has a circularity of 0.785. While the size deviations broaden with an increase in mean size across samples, the distributions of circularity and face convexity narrow as their

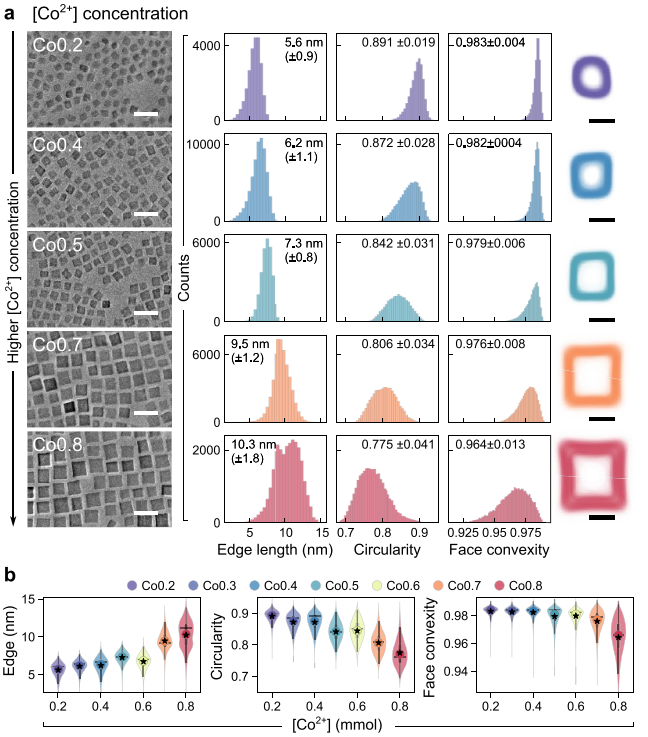

Figure 3. Statistical data of initial cobalt precursor concentration-controlled samples. a, TEM images, histograms, and contour plots of nanocrystals synthesized under cobalt concentration-controlled conditions. The water amount was kept consistent at 0.7 mL. The numbers in the sample names in the TEM images represent the amount of cobalt precursor used during the experiments; for example, 'Co0.5' refers to 0.5 mmol of $Co(ClO_4)_2$. The number of nanocrystals counted for the statistical data ranges from 24,394 to 65,404 for each sample and is listed in Table S1. Scale bars in TEM images and contour plots are 20 and 5 nm, respectively. b, Violin plots illustrating the distribution of geometric features of the nanocrystals synthesized under varying cobalt concentrations. Each violin plot includes kernel density estimation curves, representing the density of data points across the range of each feature. Additionally, mean (star), median (colored circle), and mode (horizontal black line), along with the 25−75% quartile window (gray rectangular), and 95% confidence intervals (vertical black line) are provided, offering a comprehensive visualization of the data distribution.

mean values increase. A broader or even bimodal size distribution could result from different growth stages of nanocrystals depending on the synthesis conditions. This suggests that, at the same stage, crystals formed under higher cobalt concentration may experience size defocusing, such as Ostwald ripening. The summed contour plot, visualizing the outlines of all individual nanocrystals, effectively demonstrates the trend of Co_3O_4 nanocrystals increasing in size and transitioning from a convex round shape to a concave cube as the initial concentration of the cobalt precursor increases (Methods). The trend is further supported by violin plots in Figure 3b, displaying each shape descriptor value with a density estimation for each sample. These plots reveal a strong correlation between geometric features and cobalt precursor concentrations.

Co_3O_4 nanocrystals of various morphologies can be produced through the further control of reaction kinetics by varying the oxidation conditions. When adjusting the amount of water, the nanocrystals change shape while maintaining approximately

https://doi.org/10.1021/acsnano.4c09312
ACS Nano 2024, 18, 29736−29747

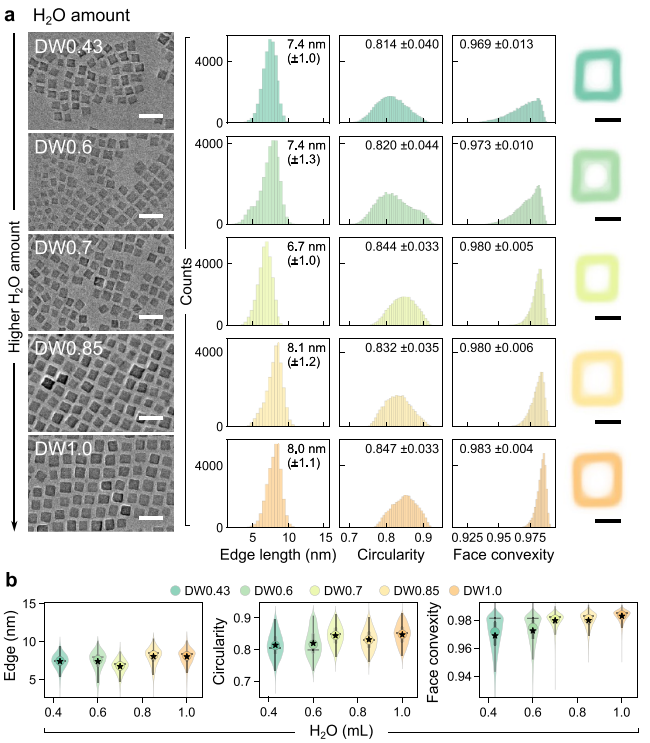

Figure 4. Statistical data of water concentration-controlled samples. a, TEM images, histograms, and contour plots of nanocrystals synthesized under water concentration-controlled conditions. $Co(ClO_4)_2$ amount was kept consistent at 0.6 mmol. The numbers in the sample names in the TEM images represent the amount of water used during the experiments; for example, 'DW0.7' refers to 0.7 mL of water. The number of nanocrystals counted for the statistical data ranges from 27,822 to 32,879 for each sample (see Table S1). b, Violin plots illustrating the distribution of geometric features of the nanocrystals synthesized under varying water amounts. A detailed description of the violin plot is provided in Figure 3. Scale bars in TEM images and contour plots are 20 and 5 nm, respectively.

similar sizes across samples (Figure 4; DW0.43−DW1.0). As the amount of water increases, both the circularity and face convexity of the nanocrystals tend to increase. Although the size distribution remains relatively unchanged, the distributions of circularity and face convexity narrow as their mean values increase. The broader shape distribution observed in samples with lower mean circularity and face convexity, compared to those with higher mean values, may be attributed to the presence of nanocrystals with both kinetic and thermodynamic shapes in the former (detailed discussion in the following section). This is supported by the statistical results presented in histograms and violin plots in Figure 4, which show that high circularity and face convexity values are present in all samples. Emergence of concave nanocrystals can be attributed to the growth behavior under water-deficient conditions. As water decreases, the hydrolysis of the metal−ligand complex is less favorable, causing premonomeric species to oxidize on the nanocrystal surface rather than in the solution due to lower activation energy for surface reaction.[38] Since the corners and edges have a higher degree of curvatures than faces, the coverage density of the surfactants is lower, resulting in easier access to growing species for the surface reaction/deposition on that site.[39−41] Therefore, surface deposition tends to occur on the corners/edges, forming higher energy surfaces.

Given the individual contributions of cobalt precursors and water in architecting the final size and shape during nanocrystal growth, it becomes crucial to understand how the interplay of experimental parameters impacts geometric features for designed synthesis. Uncovering these relationships facilitates navigating optimal synthetic conditions for nanocrystals with targeted geometric features. To estimate the size and shape of the final product from a given synthetic condition by varying cobalt precursors and water, we examined the linear relationships between the mean values of shape descriptors and different mathematical operations (multiplication, division) of the amount of synthetic parameters, including their exponentiation to various powers (Figure S6). The use of exponentiation allows us to explore the nonlinear effects and higher-order interactions of these parameters. By testing these combinations, we aimed to identify the best combination that yields the minimum R-squared value when fitted to a line, thus indicating the strongest relationship with the shape descriptors. Although there is a possibility of overfitting the data points, the general trend indicates a higher-order magnitude contribution of the cobalt precursor than water for three different shape descriptors. The dominant role of cobalt concentration in determining the size of nanocrystals is even more pronounced at high cobalt concentrations, with orders of magnitude differences. To validate this empirical model, we tested it by choosing synthesis conditions that were not used during the fit (e.g., 'Co0.5'), and the results confirmed its validity (see Figures S6 and S7).

Nanocrystal Shape Evolution through Size-Domain Analysis and Visualization. While histograms provide valuable information on the size and shape distributions of nanocrystals within a sample, they do not reveal how shape distribution varies with size. For example, histograms do not show whether smaller nanocrystals are round or concave. Scatter plots, however, are particularly useful as they not only allow for shape comparisons between different samples but also facilitate the exploration of the relationship between size and shape within nanocrystals belonging to the same sample. In these scatter plots, each data point corresponds to a single nanocrystal (Figure 5a,b and Figure S8). To avoid visualization problems when plotting multiple samples in a single scatter plot (uppermost row in Figure 5a,b), we decided, based on the empirical investigation of data size requirements, to analyze 2000 randomly selected particles per sample. This approach allowed us to effectively study the distribution of geometric features among nanocrystals under various experimental conditions. By color-coding data points based on particle size, the relationship between size, circularity, and face convexity becomes evident. This multidimensional visualization enables us to understand unobservable aspects in histograms, such as how smaller nanocrystals exhibit more round and convex shapes.

To check representative nanocrystal shapes for each sample, we selected nanocrystals with median values of shape descriptors (star symbols in scatter plots) and displayed their respective TEM images (Figure 5c,d). As seen in Figures 3 and 4, scatter plots also reveal changes in nanocrystal shape depending on synthesis conditions. Furthermore, observations from the distribution of shape information on individual particles in scatter plots and TEM images of representative particles indicate a tendency for smaller crystals, regardless of synthetic conditions, to exhibit a nearly "round" shape with higher circularity and convex surfaces. This suggests that smaller crystals attain equilibrium shapes under thermodynamic control rather than kinetic growth.

https://doi.org/10.1021/acsnano.4c09312
ACS Nano 2024, 18, 29736−29747

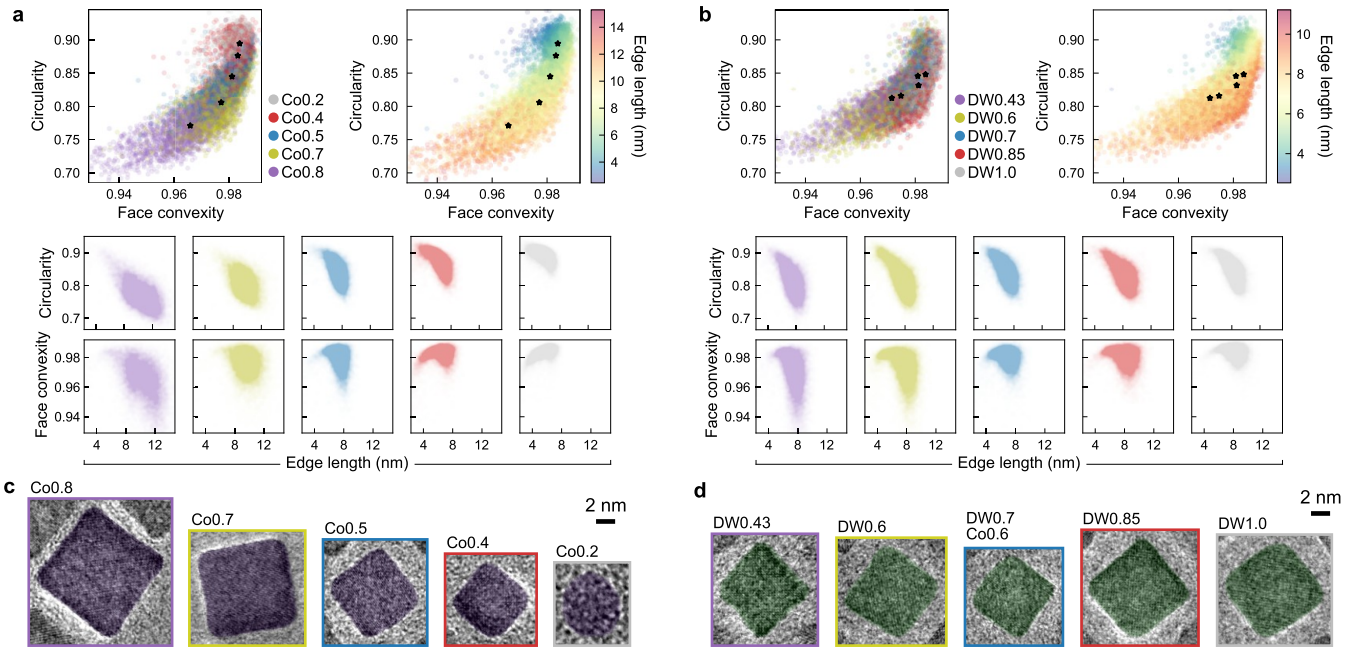

Figure 5. Shape distribution of individual nanocrystal samples under varying experimental conditions. a, b, Scatter plots showing the distributions of edge length, circularity, and face convexity for cobalt precursor concentration-controlled (a) and water amount-controlled samples (b). For the scatter plots in the uppermost row of (a) and (b), where multiple nanocrystal samples are combined in a single plot, 2000 particles were selected uniformly at random from each nanocrystal sample. Colors in the upper right plot indicate each nanocrystal's edge length value and colors in the rest of the plots indicate the type of sample. Star symbols denote the median values of each sample. c, d, TEM images showing the representative shape of nanocrystals, with particle regions segmented and highlighted in purple for cobalt-controlled (c) and in green for water-controlled (d). Representative particles were selected based on the median values of shape descriptors for each sample.

To delve deeper into these observations and clarify the comparison between different synthesis conditions, we generated size-domain scatter plots to illustrate changes in circularity and face convexity values at 0.2 nm size intervals (Figure 6a). These plots allow for quantitative comparisons of how nanocrystal shapes evolve with varying monomer concentrations within the same size domain. From this analysis, we inferred that the influence of synthetic conditions on nanoparticle shape varies with particle size. Within the size range of 4.3−5.3 nm, the mean values of circularity and face convexity remain high, close to 0.90 and 0.985, respectively, and do not vary across synthesis conditions, as indicated by the low CVs of mean values. This consistency is observed when varying Co concentration, as well as when varying water concentration. At larger nanocrystal sizes, different shape descriptor values begin to emerge for each synthesis condition. For instance, at 4.3 nm, the circularity and face convexity values of cobalt-controlled samples are similar, but for sizes above 5.3 nm, differences in shape between samples become more pronounced as the size increases. Similar trends are observed in the water-controlled experimental groups. Again, this can be seen by the increase of CV across mean values starting at around 4.3 nm.

The sizes at which both shape properties reach their maximum values are 4.3 nm for circularity and 5.3−6.5 nm for face convexity, with the latter peaking at larger sizes. This indicates that crystals predominantly exhibit a round shape at 4.3 nm. Within the 4.3−5.3 nm range, face convexity slightly increases or remains similar, while circularity decreases, suggesting that crystals begin creating facets from a round shape. Samples with a significant decrease in face convexity values at sizes above the 5.3 nm range (i.e., 'Co0.8', 'DW0.43', 'DW0.6') indicate that at this critical size the crystals begin to have concave surfaces. To visually depict this phenomenon, we use contours to plot the shape probability distribution of nanocrystals for each size-domain, providing a comprehensive understanding of shape evolution (Figure 6b) (see Figure S9 for representative TEM images and Figure S10 for the effect of data size on the size-resolved analysis). Contour plots of nanocrystals within the 4.3−5.3 nm range exhibit relatively small changes in mean circularity and face convexity values between samples, representing similar round shapes (Figure 6b). As size increases, the difference in contour shape across experimental conditions becomes more pronounced. For instance, the 'DW0.43' and 'DW1.0' samples at 4.3 nm exhibit similar round shapes, but at 8.5 nm, 'DW0.43' features concave surfaces while 'DW1.0' has truncated corners.

The "Onset Radius": Thermodynamic and Kinetic Control during Nanocrystal Growth. This phenomenon—the shape transition from round shapes at smaller sizes to faceted shapes at larger sizes—can be attributed to the variance in surface-to-volume ratio among the polyhedra with different facets, which varies with crystal size. For spinel transition metal oxides, the surface energies of low-index facets typically follow the order $\gamma_{\{100\}} < \gamma_{\{110\}} < \gamma_{\{111\}}$.[42−44] Due to this facet-dependent surface energy, Co_3O_4 nanocrystals are expected to adopt a cubic shape. However, when nanocrystals are as small as sub-10 nm scales, the surface-to-volume ratio increases significantly, contributing more to minimizing the overall energy. To minimize the total free energy of the crystal, the surface tends to form a structure with the lowest surface-to-volume ratio, leading to rounded shapes for small crystals rather than faceted ones. As the crystal size increases to a certain extent, faceted surfaces become energetically advantageous for lowering the total energy, leading to the adoption of faceted structures. As explained by the Wulff theorem, the relationship (γ/d = constant) between the specific surface free energy (γ) and the

https://doi.org/10.1021/acsnano.4c09312
ACS Nano 2024, 18, 29736−29747

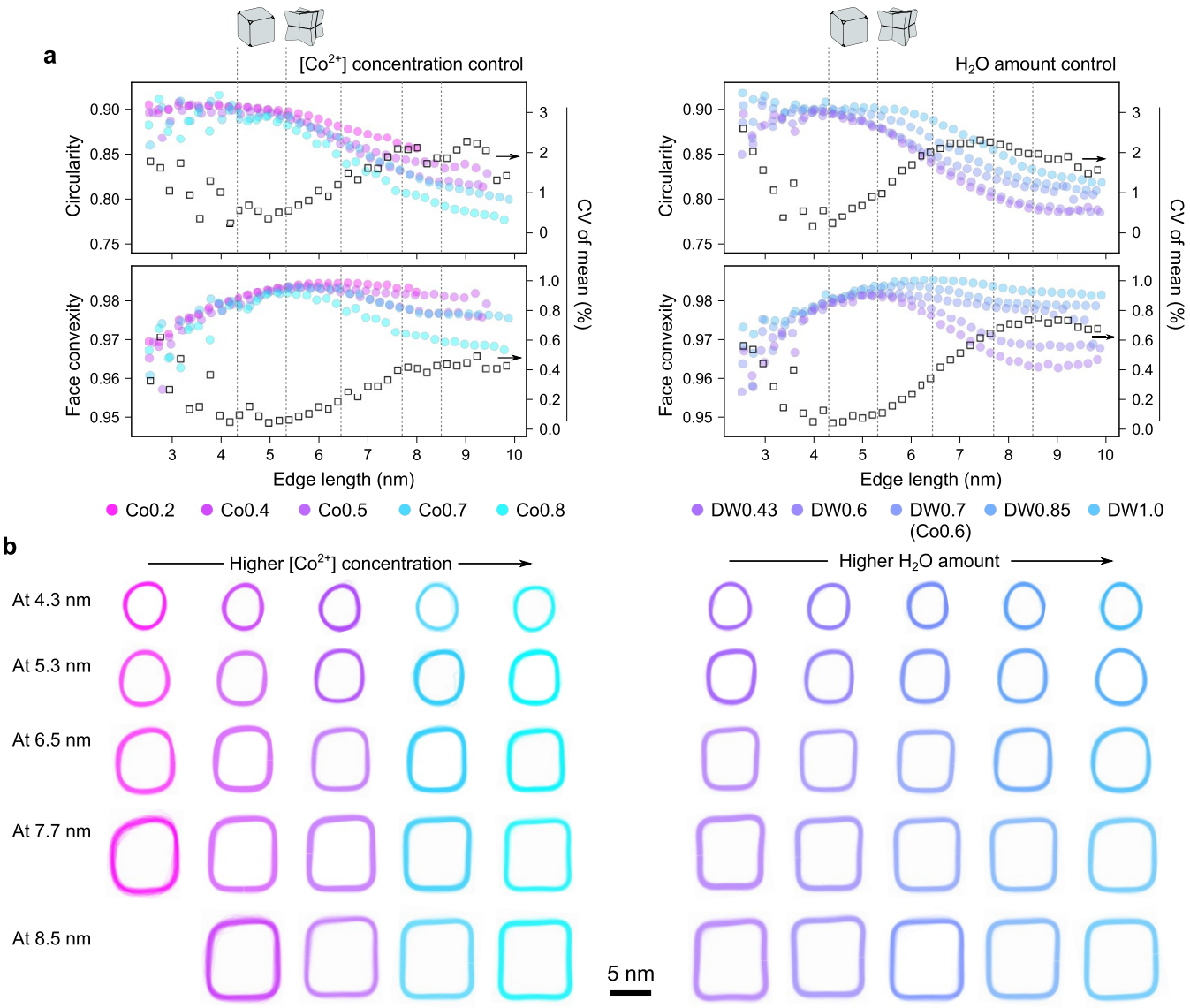

Figure 6. Size-resolved shape probability distributions of nanocrystals. a, Comparison of mean and CV values for nanocrystal samples in different size domains. Colored circles represent the mean values of nanocrystal samples, while hollow black squares indicate the CV values between these means. Vertical lines in the plots indicate edge lengths of 4.3, 5.3, 6.5, 7.7, and 8.5 nm. b, Size-domain contour plots of nanocrystals. These plots enable comparison of average shape distributions based on size and variations in shape across different experimental conditions as size increases.

distance from the facet to the crystal center (d) causes {100}, {110}, and {111} facets to appear as truncated polyhedral, reducing the total surface energy of the crystals. This explains the decrease in circularity beyond a certain size, resulting in shapes such as truncated octahedra and cubes. Up to this point, crystal growth appears to be controlled by thermodynamics.

Furthermore, as crystals grow larger, they acquire lower energy due to the contribution of volume energy, allowing them to accommodate relatively high-energy surfaces. Our research shows that, consequently, face convexity gradually decreases in the range of approximately 5.3−8.5 nm. Beyond 8.5 nm, face convexity no longer decreases significantly with increasing size, indicating a balance between surface energy and volume energy in determining the total free energy, resulting in a relatively constant facet ratio on the surface. In this kinetically controlled growth regime, facets start to be determined by the growth rate of each face, with the growth rate of high-energy facets being much faster than that of low-energy facets. As a result, crystals grow more rapidly along the ⟨111⟩ direction, forming concave surfaces with high-index facets (see 'Co0.8' and 'DW0.43' in Figure 6).[45]

We propose the concept of the "onset radius" to describe two critical size thresholds in the formation of Co_3O_4 nanocrystals in this study: the onset of surface faceting and the onset of kinetic crystal growth. The former represents a size threshold at which the surface energy difference between facets predominantly governs the total surface free energy of crystallites, leading to the development of faceted crystals. Within the size range of 4.3 nm, all samples exhibit similar circularity and face convexity, with minimal differences in mean values and a CV of less than 1% among samples, indicating uniform shape consistency across the entire sample set. As crystals grow beyond 4.3 nm, circularity gradually decreases while face convexity either remains constant or increases, marking the onset of crystal surface faceting and defining this criterion as the first onset radius. At an edge length of 5.3 nm, face convexity values begin to decrease, with the

https://doi.org/10.1021/acsnano.4c09312
ACS Nano 2024, 18, 29736−29747

extent of reduction varying among samples, as evidenced by the increase in CV values, thus defining this point as the second onset radius. Below this onset, crystal growth is thermodynamically regulated, while above it, kinetic control dominates. Nanocrystal shaping becomes more evident beyond this second onset radius, serving as an indicator for high-energy surface formation, and crystals start to exhibit kinetic shapes rather than thermodynamically stable ones. Up to an edge length of 8 nm, the influence of synthesis parameters on crystal shaping is maximized as crystal size increases. Beyond this point, crystal shapes remain similar to those at 8 nm, implying that the impact of monomer concentration on crystal shape remains consistent regardless of size thereafter.

The identification and naming of these two regimes provide an opportunity for similar observations in other nanocrystal systems, within our framework. Our approach sets the stage for future research to explore the generalizability of the onset radius concept. This size-resolved analysis provides a detailed framework for examining nanocrystal growth, exploring how these regimes align with traditional growth models and vary based on different growth mechanisms. Additionally, in recent nanomaterials science, machine learning has shown great potential for finding patterns and trends in complex data, discovering new materials, and predicting properties to gain deeper insights into systems.[46−51] Leveraging large data sets will enable more effective and reliable machine learning-based analysis, further enhancing the understanding of these growth regimes. By unlocking numerous unexplored areas in nanoscience, our approach drives significant advancements in well-optimized nanocrystal synthesis.

CONCLUSIONS

In summary, our study elucidates the intricate relationship between synthesis conditions and the size and shape evolution of colloidal nanocrystals. Given the historical importance of statistics in advancing knowledge, it is crucial to incorporate robust statistical characterization into scientific findings at the nanoscale. By integrating deep learning-assisted high-throughput techniques with advanced statistical analysis, we have uncovered insights into the growth regimes governing nanocrystal morphology through a size-resolved approach. This methodology allows us to quantify subtle morphological differences across size ranges that have previously been challenging to capture experimentally. Enabled by size-resolved observations, our findings highlight the critical roles of thermodynamic and kinetic growth regimes in shaping nanocrystals. This is particularly evidenced by the observed transitions from faceted to kinetically driven growth regimes in Co_3O_4 nanocrystals. Moreover, the introduction of the "onset radius" concept offers a valuable framework for understanding the critical size thresholds at which these transitions—namely surface faceting and the formation of kinetic shapes with concave surfaces—occur. Notably, this shape evolution, captured at a singular time point under specific synthetic conditions, represents an approach that moves beyond traditional methods commonly used in nanoscience, transforming raw data into meaningful insights. By elucidating the interplay between synthesis parameters and nanocrystal morphology, our work offers a more precise understanding of nanocrystal growth and provides valuable insights into refined guidance for optimizing nanomaterial synthesis. Ultimately, these insights will guide the creation of tailored nanomaterials with enhanced properties and functionalities.

METHODS

Preparation for TEM Sample and Image Acquisition of Co_3O_4 Nanocrystals. Spinel cobalt oxide nanocrystals were synthesized using the previously reported method with a slight modification.[23] A mixture of 0.07−0.29 g of cobalt(II) perchlorate (Aldrich) in 15 mL of 1-octanol (Aldrich) and 2.67 g of oleylamine (Acros) was heated to 120 °C under air. Distilled water (0.7 mL) was added to the mixture at 80 °C during heating and aged at 120 °C for 6 h. The reaction was quenched, and the temperature was reduced to room temperature. The nanocrystals were purified with an excess amount of acetone for the first purification step and hexane/ethanol for the second purification step. At each step, the nanocrystals were retrieved by centrifugation. After emptying the supernatant, the nanocrystals were redispersed in toluene for drop casting onto the TEM grid with carbon substrate. High-resolution TEM images were collected using the aberration-corrected TEAM 0.5 microscope at the National Center for Electron Microscopy (NCEM) in the Molecular Foundry. Images of 4096 × 4096 pixels were acquired at 300 kV with the Gatan OneView camera. Magnification used for imaging was 78 kX (corresponding to 0.086 nm/pixel) and the electron dosage was set between 370 and 500 e/Å^2. This magnification was chosen to balance field of view and resolution, ensuring that lattice planes were visible while capturing a large population of nanoparticles. Each image contained between 350 and 1000 particles, depending on their size and distribution. Building on our group's prior work,[17,52] we kept the electron dosage within a similar range for all samples and imaging sessions and applied data preprocessing techniques, such as pixel value rescaling and flat-field correction, to enhance the generalization of the trained neural network across the samples. The electron dose range was selected to maintain a signal-to-noise ratio that ensures accurate segmentation, while avoiding the risk of nanoparticle damage or surface reconstruction at higher doses.

Neural Network Training. The neural network was trained using computational resources provided by the National Energy Research Scientific Computing Center (NERSC). Specifically, a GPU node was utilized to accelerate the training process. In our neural network training, we utilized an 8-fold cross-validation approach with a batch size of 8 and trained the models for 100 epochs with no early stopping. We used an initial learning rate of 0.04, applying an exponential decay with a decay rate of 0.5 every 20 epochs. To augment the training data, we used *ImageDataGenerator* in *Keras* to randomly flip individual images horizontally and/or vertically every epoch. As input data, we utilized 992 image patches, each with dimensions of 512 × 512 pixels. Input images were chosen from 'Co0.4' (864 patches with pixel size 33−67 pm), 'Co0.6' (64 patches with pixel size 67 pm), and 'Co0.7' (64 patches with pixel size 86 pm). Input data were split into training and validation sets in an 8:1 ratio, ensuring a balanced and representative distribution. The U-Net architecture with a ResNet-18 backbone was initialized and compiled with the Adam optimizer and a combined categorical cross-entropy and Dice coefficient loss function (Details can be found in our code implementation, available at https://github.com/ScottLabUCB). Metrics used to assess the model's performance at each epoch included the Intersection over Union (IoU) score and the F1 score (see Figure S2 for the learning curve during training).

$$\text{F1 score} = \frac{\text{TP}}{\text{TP} + 0.5(\text{FN} + \text{FP})}$$

TP (true positive) indicates correct identification of particle regions, FP (false positive) denotes misidentification of background as particle regions, and FN (false negative) represents particle regions mistakenly identified as background. The F1 score calculates the harmonic mean of precision (=TP/(TP+FP)) and recall (=TP/(TP+FN)), equally weighs the contribution of both metrics. The best possible F1 score is 1, indicating a perfect model where all predictions are correct, and the worst is 0, reflecting no correct predictions.

Testing the Images with Trained Neural Network for Particle Predictions. To test new images not used during the training and validation process, we selected the trained neural network with the lowest validation loss from the 8-fold cross validation study as the best-performing model. Its performance was evaluated with 512 × 512 image

https://doi.org/10.1021/acsnano.4c09312
ACS Nano 2024, 18, 29736−29747

patches of 'Co0.5' with pixel size of 86 pm using the soft Dice coefficient, which was displayed in a confusion matrix (see Figure S2). The best performing model, saved during the training, then predicted the particle and background regions for unseen test data (4k resolution images) individually at a speed of less than 0.1 s/image using the computational resources of NERSC. The results were stored in an array, and the predicted images were saved for further analysis.

Postprocessing of Predicted Images. To refine the segmentation masks predicted by the neural network, we implemented a postprocessing pipeline that involved thresholding, connected component analysis for individual particle identification, and edge-touching region removal. The predicted images consisted of values ranging from 0 to 1 due to the use of the softmax function during the testing phase. Therefore, for each predicted segmentation mask, a threshold of 0.5 was applied to generate a binary image, where pixels with a probability greater than 0.5 were marked as particles, and others as background. The threshold value of 0.5 was selected based on statistical results, demonstrating the reasonable match between the predicted regions and the ground truth data (Figure S2). Connected component analysis was then performed to label each particle in the binary images. Subsequently, we filtered out any "edge-touching regions", or regions in the predicted mask that touch the image boundaries, often resulting in incomplete or partially visible objects. By filtering these out, we ensure only fully contained and well-defined particles are retained, enhancing segmentation accuracy and reliability. This was achieved by analyzing the bounding box coordinates of each labeled region. Regions with bounding boxes at the image boundaries were excluded, ensuring only complete particles within the image boundaries were retained.

Feature Extraction and Filtering. Scikit-image package was used to calculate the properties of regions identified as individual particles. For each region, the area was calculated by multiplying the pixel area by the square of the pixel size, converting it into actual square units. Subsequently, each object underwent a series of conditional checks to determine its eligibility as a particle based on the following criteria (see Figure S3 and Table S2): the area must fall within predefined lower (6 nm^2) and upper bounds (which vary across different samples); the eccentricity, indicating the elongation of the shape, must be below a set upper threshold; and the solidity, referred to here as face convexity, which measures compactness, must surpass a lower threshold. If an object met all these conditions, further shape analysis was conducted. We computed the perimeter of its convex hull and then calculated the convexity—the convex hull perimeter divided by the object's perimeter. If this ratio exceeded the specified lower bound, we kept the object's label in the image at that location. This approach only selected particles that met all required geometrical standards as regular particles for further analysis, including geometrical feature measurements and contour extractions.

Generation of Contour Plots. For each particle identified within labeled images, contours were extracted using the *find_contours* function in the scikit-image package, tracing the exterior boundaries of objects. The extracted contours were used without any postprocessing such as smoothing. On average, the contours contained between 300 and 585 points, depending on the size of the nanoparticles. To analyze and compare the contours, we reparameterized the contours from a list of Cartesian coordinates (x, y) to a radial coordinate (r, θ) system. In this system, the radial coordinate represents the contour as the Euclidean distance and angle from the centroid, which is the center of the contour. To visualize the average shape of nanocrystals within a given subset, we plotted the sum of the contours of the nanocrystals. To align these contours to a consistent orientation,[53] an initial contour was selected as a reference orientation. Each subsequent contour was then permuted through all possible orientations, including rotations and mirroring to account for opposite chirality (i.e., particles flipped upside down). For each permutation, the Euclidean distance to the running average shape, computed from the already aligned contours, was calculated. The permutation with the smallest distance to the running average shape was chosen as the aligned orientation for that shape. This process was repeated iteratively, updating the running average shape with each newly aligned contour, resulting in a set of contours that are consistently oriented relative to one another.

ASSOCIATED CONTENT

Supporting Information

The Supporting Information is available free of charge at https://pubs.acs.org/doi/10.1021/acsnano.4c09312.

Table of nanocrystal samples synthesized under various experimental conditions, examples of 4k full resolution images for nanocrystal samples, before and after the filtering of unwanted images in predicted images, relationships between shape properties and synthetic parameters, and comparisons of statistical results depending on the data size (PDF)

AUTHOR INFORMATION

Corresponding Authors

Min Gee Cho − *National Center for Electron Microscopy, Molecular Foundry, Lawrence Berkeley National Laboratory, Berkeley, California 94720, United States; Department of Materials Science and Engineering, University of California Berkeley, Berkeley, California 94720, United States;* orcid.org/0000-0003-4490-7352; Email: mgcho@lbl.gov

Mary C. Scott − *National Center for Electron Microscopy, Molecular Foundry, Lawrence Berkeley National Laboratory, Berkeley, California 94720, United States; Department of Materials Science and Engineering, University of California Berkeley, Berkeley, California 94720, United States;* Email: mary.scott@berkeley.edu

Authors

Katherine Sytwu − *National Center for Electron Microscopy, Molecular Foundry, Lawrence Berkeley National Laboratory, Berkeley, California 94720, United States*

Luis Rangel DaCosta − *National Center for Electron Microscopy, Molecular Foundry, Lawrence Berkeley National Laboratory, Berkeley, California 94720, United States; Department of Materials Science and Engineering, University of California Berkeley, Berkeley, California 94720, United States;* orcid.org/0000-0001-8966-0408

Catherine Groschner − *Department of Materials Science and Engineering, University of California Berkeley, Berkeley, California 94720, United States;* orcid.org/0000-0001-9996-1124

Myoung Hwan Oh − *Department of Energy Engineering, KENTECH Institute for Environmental and Climate Technology, Korea Institute of Energy Technology, Naju 58330, Republic of Korea;* orcid.org/0000-0002-8338-3881

Complete contact information is available at: https://pubs.acs.org/10.1021/acsnano.4c09312

Author Contributions

M.G.C. and M.C.S. conceived and designed the project; M.G.C. synthesized the cobalt oxide nanocrystals, carried out the TEM imaging, conducted neural network training and testing, modified neural network script for model optimization, and wrote scripts for image prediction and statistical analysis of identified nanocrystals in TEM images; M.H.O. advised nanocrystal synthesis and TEM sample preparation; K.S. provided the script for the flat-field correction and alignment of contours; L.R.D. helped with solving computational and

https://doi.org/10.1021/acsnano.4c09312
ACS Nano 2024, 18, 29736−29747

coding issues; C.G. developed the neural network architecture; M.G.C. wrote the original draft. M.G.C., K.S., L.R.D., M.H.O., and M.C.S. revised and commented on the manuscript.

Notes

The authors declare no competing financial interest.

ACKNOWLEDGMENTS

M.G.C. is grateful to Colin Ophus for useful discussions, to Peter Ercius and Chengyu Song for help with using TEAM0.5 instrument. Work at the Molecular Foundry was supported by the Office of Science, Office of Basic Energy Sciences, of the U.S. Department of Energy under Contract No. DE-AC02-05CH11231. This research used resources of the National Energy Research Scientific Computing Center (NERSC), a U.S. Department of Energy Office of Science User Facility located at Lawrence Berkeley National Laboratory, operated under Contract No. DE-AC02-05CH11231 using NERSC award BES-ERCAP0026467. M.C.S. and M.G.C. are funded by the U.S. Department of Energy in the program "4D Camera Distillery: From Massive Electron Microscopy Scattering Data to Useful Information with AI/ML. M.G.C. also acknowledges Basic Science Research Program through the National Research Foundation of Korea (NRF) funded by the Ministry of Education (2021R1A6A3A14045275). M.H.O. is supported by the Korea Institute of Energy Technology Evaluation and Planning (KETEP) and the Ministry of Trade, Industry & Energy (MOTIE) of the Republic of Korea (No. 20224000000320). K.S. was supported by an appointment to the Intelligence Community Postdoctoral Research Fellowship Program at Lawrence Berkeley National Laboratory administered by Oak Ridge Institute for Science and Education (ORISE) through an interagency agreement between the US Department of Energy and the Office of the Director of National Intelligence (ODNI). L.R.D. is supported by the U.S. Department of Energy, Office of Science, Office of Advanced Scientific Computing Research, Department of Energy Computational Science Graduate Fellowship under Award Number DE-SC0021110.

REFERENCES

(1) Murray, C. B.; Norris, D. J.; Bawendi, M. G. Synthesis and Characterization of Nearly Monodisperse CdE (E = Sulfur, Selenium, Tellurium) Semiconductor Nanocrystallites. *J. Am. Chem. Soc.* **1993**, *115*, 8706−8715.

(2) Peng, X.; Manna, L.; Yang, W.; Wickham, J.; Scher, E.; Kadavanich, A.; Alivisatos, A. P. Shape Control of CdSe Nanocrystals. *Nature* **2000**, *404*, 59−61.

(3) Katari, J. E. B.; Colvin, V. L.; Alivisatos, A. P. X-Ray Photoelectron Spectroscopy of CdSe Nanocrystals with Applications to Studies of the Nanocrystal Surface. *J. Phys. Chem. A* **1994**, *98*, 4109−4117.

(4) Skrabalak, S. E. Symmetry in Seeded Metal Nanocrystal Growth. *Acc. Mater. Res.* **2021**, *2*, 621−629.

(5) Talapin, D. V.; Lee, J.-S.; Kovalenko, M. V.; Shevchenko, E. V. Prospects of Colloidal Nanocrystals for Electronic and Optoelectronic Applications. *Chem. Rev.* **2010**, *110*, 389−458.

(6) Kang, J.; Sherman, Z. M.; Conrad, D. L.; Crory, H. S. N.; Dominguez, M. N.; Valenzuela, S. A.; Anslyn, E. V.; Truskett, T. M.; Milliron, D. J. Structural Control of Plasmon Resonance in Molecularly Linked Metal Oxide Nanocrystal Gel Assemblies. *ACS Nano* **2023**, *17*, 24218−24226.

(7) Xie, C.; Niu, Z.; Kim, D.; Li, M.; Yang, P. Surface and Interface Control in Nanoparticle Catalysis. *Chem. Rev.* **2020**, *120*, 1184−1249.

(8) Yin, A. X.; Min, X. Q.; Zhang, Y. W.; Yan, C. H. Shape-Selective Synthesis and Facet-Dependent Enhanced Electrocatalytic Activity and Durability of Monodisperse Sub-10 Nm Pt-Pd Tetrahedrons and Cubes. *J. Am. Chem. Soc.* **2011**, *133*, 3816−3819.

(9) Xie, X.; Li, Y.; Liu, Z.-Q.; Haruta, M.; Shen, W. Low-Temperature Oxidation of CO Catalysed by Co_3O_4 Nanorods. *Nature* **2009**, *458*, 746−749.

(10) Haase, F. T.; Bergmann, A.; Jones, T. E.; Timoshenko, J.; Herzog, A.; Jeon, H. S.; Rettenmaier, C.; Cuenya, B. R. Size Effects and Active State Formation of Cobalt Oxide Nanoparticles during the Oxygen Evolution Reaction. *Nat. Energy* **2022**, *7*, 765−773.

(11) Wang, X.; Li, J.; Ha, H. D.; Dahl, J. C.; Ondry, J. C.; Moreno-Hernandez, I.; Head-Gordon, T.; Alivisatos, A. P. AutoDetect-MNP: An Unsupervised Machine Learning Algorithm for Automated Analysis of Transmission Electron Microscope Images of Metal Nanoparticles. *JACS Au* **2021**, *1*, 316−327.

(12) Lee, B.; Yoon, S.; Lee, J. W.; Kim, Y.; Chang, J.; Yun, J.; Ro, J. C.; Lee, J.-S.; Lee, J. H. Statistical Characterization of the Morphologies of Nanoparticles through Machine Learning Based Electron Microscopy Image Analysis. *ACS Nano* **2020**, *14*, 17125−17133.

(13) Gumbiowski, N.; Loza, K.; Heggen, M.; Epple, M. Automated Analysis of Transmission Electron Micrographs of Metallic Nanoparticles by Machine Learning. *Nanoscale Adv.* **2023**, *5*, 2318−2326.

(14) Visheratina, A.; Visheratin, A.; Kumar, P.; Veksler, M.; Kotov, N. A. Chirality Analysis of Complex Microparticles using Deep Learning on Realistic Sets of Microscopy Images. *ACS Nano* **2023**, *17*, 7431−7442.

(15) Moen, E.; Bannon, D.; Kudo, T.; Graf, W.; Covert, M.; Van Valen, D. Deep Learning for Cellular Image Analysis. *Nat. Methods* **2019**, *16*, 1233−1246.

(16) Groschner, C. K.; Choi, C.; Scott, M. C. Machine Learning Pipeline for Segmentation and Defect Identification from High-Resolution Transmission Electron Microscopy Data. *Microsc. Microanal.* **2021**, *27*, 549−556.

(17) Sytwu, K.; Rangel DaCosta, L.; Scott, M. C. Generalization Across Experimental Parameters in Neural Network Analysis of High-Resolution Transmission Electron Microscopy Datasets. *Microsc. Microanal.* **2024**, *30*, 85−95.

(18) Bals, J.; Epple, M. Deep Learning for Automated Size and Shape Analysis of Nanoparticles in Scanning Electron Microscopy. *RSC Adv.* **2023**, *13* (5), 2795−2802.

(19) Neumann, S.; Rezvani, A.; Barasinski, M.; Garnweitner, G.; Segets, D.; Rafaja, D. Statistical Determination of Atomic-Scale Characteristics of Au Nanocrystals Based on Correlative Multiscale Transmission Electron Microscopy. *Microsc. Microanal.* **2023**, *29*, 118−130.

(20) Koolen, C. D.; Torrent, L.; Agarwal, A.; Meili-Borovinskaya, O.; Gasilova, N.; Li, M.; Luo, W.; Züttel, A. High-Throughput Sizing, Counting, and Elemental Analysis of Anisotropic Multimetallic Nanoparticles with Single-Particle Inductively Coupled Plasma Mass Spectrometry. *ACS Nano* **2022**, *16*, 11968−11978.

(21) Braham, E. J.; Cho, J.; Forlano, K. M.; Watson, D. F.; Arròyave, R.; Banerjee, S. Machine Learning-Directed Navigation of Synthetic Design Space: A Statistical Learning Approach to Controlling the Synthesis of Perovskite Halide Nanoplatelets in the Quantum-Confined Regime. *Chem. Mater.* **2019**, *31*, 3281−3292.

(22) Piella, J.; Bastús, N. G.; Puntes, V. Size-Controlled Synthesis of Sub-10-Nanometer Citrate-Stabilized Gold Nanoparticles and Related Optical Properties. *Chem. Mater.* **2016**, *28*, 1066−1075.

(23) Oh, M. H.; Cho, M. G.; Chung, D. Y.; Park, I.; Kwon, Y. P.; Ophus, C.; Kim, D.; Kim, M. G.; Jeong, B.; Gu, X. W.; Jo, J.; Yoo, J. M.; Hong, J.; McMains, S.; Kang, K.; Sung, Y. E.; Alivisatos, A. P.; Hyeon, T. Design and Synthesis of Multigrain Nanocrystals via Geometric Misfit Strain. *Nature* **2020**, *577*, 359−363.

(24) Han, X.; He, G.; He, Y.; Zhang, J.; Zheng, X.; Li, L.; Zhong, C.; Hu, W.; Deng, Y.; Ma, T. Y. Engineering Catalytic Active Sites on Cobalt Oxide Surface for Enhanced Oxygen Electrocatalysis. *Adv. Energy Mater.* **2018**, *8* (10), No. 1702222.

(25) Song, K.; Cho, E.; Kang, Y. M. Morphology and Active-Site Engineering for Stable Round-Trip Efficiency Li-O2 Batteries: A Search

https://doi.org/10.1021/acsnano.4c09312
ACS Nano 2024, 18, 29736−29747

for the Most Active Catalytic Site in Co_3O_4. *ACS Catal.* **2015**, *5*, 5116−5122.
(26) Liu, L.; Jiang, Z.; Fang, L.; Xu, H.; Zhang, H.; Gu, X.; Wang, Y. Probing the Crystal Plane Effect of Co_3O_4 for Enhanced Electrocatalytic Performance toward Efficient Overall Water Splitting. *ACS Appl. Mater. Interfaces* **2017**, *9*, 27736−27744.
(27) Dong, Y.; He, K.; Yin, L.; Zhang, A. A Facile Route to Controlled Synthesis of Co_3O_4 Nanoparticles and Their Environmental Catalytic Properties. *Nanotechnology* **2007**, *18*, No. 435602.
(28) He, K.; Zhang, X.; Ren, S.; Sun, J.Deep residual learning for image recognition. In *2016 IEEE Conference on Computer Vision and Pattern Recognition (CVPR)*; IEEE, 2016; pp 770−778 .
(29) Ronneberger, O.; Fischer, P.; Brox, T.U-Net: Convolutional networks for biomedical image segmentation. In *Medical Image Computing and Computer-Assisted Intervention−MICCAI 2015*, Lecture Notes in Computer Science; Springer International Publishing, 2015; Vol. *9351*, pp 234−241 DOI: 10.1007/978-3-319-24574-4_28.
(30) Sytwu, K.; Groschner, C.; Scott, M. C. Understanding the Influence of Receptive Field and Network Complexity in Neural Network-Guided TEM Image Analysis. *Microsc. Microanal.* **2022**, *28*, 1896−1904.
(31) Grzelczak, M.; Zhang, J.; Pfrommer, J.; Hartmann, J.; Driess, M.; Antonietti, M.; Wang, X. Electro- and Photochemical Water Oxidation on Ligand-Free Co_3O_4 Nanoparticles with Tunable Sizes. *ACS Catal.* **2013**, *3*, 383−388.
(32) Jung, S.-K.; Kim, H.; Cho, M. G.; Cho, S.-P.; Lee, B.; Kim, H.; Park, Y.-U.; Hong, J.; Park, K.; Yoon, G.; Seong, W. M.; Cho, Y.; Oh, M. H.; Kim, H.; Gwon, H.; Hwang, I.; Hyeon, T.; Yoon, W.-S.; Kang, K. Lithium-Free Transition Metal Monoxides for Positive Electrodes in Lithium-Ion Batteries. *Nat. Energy* **2017**, *2*, No. 16208.
(33) Oh, M. H.; Yu, T.; Yu, S.-H.; Lim, B.; Ko, K.-T.; Willinger, M.-G.; Seo, D.-H.; Kim, B. H.; Cho, M. G.; Park, J.-H.; Kang, K.; Sung, Y.-E.; Pinna, N.; Hyeon, T. Galvanic Replacement Reactions in Metal Oxide Nanocrystals. *Science* **2013**, *340*, 964−968.
(34) Calvin, J. J.; Brewer, A. S.; Alivisatos, A. P. The Role of Organic Ligand Shell Structures in Colloidal Nanocrystal Synthesis. *Nat. Synth.* **2022**, *1*, 127−137.
(35) Mourdikoudis, S.; Liz-Marzán, L. M. Oleylamine in Nanoparticle Synthesis. *Chem. Mater.* **2013**, *25*, 1465−1476.
(36) Owen, J. S.; Chan, E. M.; Liu, H.; Alivisatos, A. P. Precursor Conversion Kinetics and the Nucleation of Cadmium Selenide Nanocrystals. *J. Am. Chem. Soc.* **2010**, *132*, 18206−18213.
(37) Parashar, M.; Shukla, V. K.; Singh, R. Metal Oxides Nanoparticles via Sol−Gel Method: A Review on Synthesis, Characterization and Applications. *J. Mater. Sci. Mater. Electron.* **2020**, *31*, 3729−3749.
(38) Yang, T. H.; Zhou, S.; Gilroy, K. D.; Figueroa-Cosme, L.; Lee, Y. H.; Wu, J. M.; Xia, Y. Autocatalytic Surface Reduction and Its Role in Controlling Seed-Mediated Growth of Colloidal Metal Nanocrystals. *Proc. Natl. Acad. Sci. U. S. A.* **2017**, *114*, 13619−13624.
(39) Li, Y.; Lin, H.; Zhou, W.; Sun, L.; Samanta, D.; Mirkin, C. A. Corner-, Edge-, and Facet-Controlled Growth of Nanocrystals. *Sci. Adv.* **2021**, *7* (3), No. eabf1410.
(40) Janicek, B. E.; Hinman, J. G.; Hinman, J. J.; Bae, S. H.; Wu, M.; Turner, J.; Chang, H. H.; Park, E.; Lawless, R.; Suslick, K. S.; Murphy, C. J.; Huang, P. Y. Quantitative Imaging of Organic Ligand Density on Anisotropic Inorganic Nanocrystals. *Nano Lett.* **2019**, *19*, 6308−6314.
(41) Ye, X.; Jones, M. R.; Frechette, L. B.; Chen, Q.; Powers, A. S.; Ercius, P.; Dunn, G.; Rotskoff, G. M.; Nguyen, S. C.; Adiga, V. P.; Zettl, A.; Rabani, E.; Geissler, P. L.; Alivisatos, A. P. Single-Particle Mapping of Nonequilibrium Nanocrystal Transformations. *Science* **2016**, *354*, 874−877.
(42) Hu, L.; Peng, Q.; Li, Y. Selective Synthesis of Co_3O_4 Nanocrystal with Different Shape and Crystal Plane Effect on Catalytic Property for Methane Combustion. *J. Am. Chem. Soc.* **2008**, *130*, 16136−16137.
(43) Su, D.; Dou, S.; Wang, G. Single Crystalline Co_3O_4 Nanocrystals Exposed with Different Crystal Planes for Li-O2 Batteries. *Sci. Rep.* **2014**, *4*, No. 5767.
(44) Ribeiro, R. A. P.; de Lazaro, S. R.; Gracia, L.; Longo, E.; Andrés, J. Theoretical Approach for Determining the Relation between the Morphology and Surface Magnetism of Co_3O_4. *J. Magn. Magn. Mater.* **2018**, *453*, 262−267.
(45) Yin, Y.; Alivisatos, A. P. Colloidal Nanocrystal Synthesis and the Organic−Inorganic Interface. *Nature* **2005**, *437*, 664−670.
(46) Lin, R.; Zhang, R.; Wang, C.; Yang, X.-Q.; Xin, H. L. TEMImageNet training library and AtomSegNet deep-learning models for high-precision atom segmentation, localization, denoising, and deblurring of atomic-resolution images. *Sci. Rep.* **2021**, *11*, No. 5386.
(47) Dahl, J. C.; Niblett, S.; Cho, Y.; Wang, X.; Zhang, Y.; Chan, E. M.; Alivisatos, A. P. Scientific Machine Learning of 2D Perovskite Nanosheet Formation. *J. Am. Chem. Soc.* **2023**, *145*, 23076−23087.
(48) Torrisi, S. B.; Bazant, M. Z.; Cohen, A. E.; Cho, M. G.; Hummelshøj, J. S.; Hung, L.; Kamat, G.; Khajeh, A.; Kolluru, A.; Lei, X.; Ling, H.; Montoya, J. H.; Mueller, T.; Palizhati, A.; Paren, B. A.; Phan, B.; Pietryga, J.; Sandraz, E.; Schweigert, D.; Shao-Horn, Y.; Trewartha, A.; Zhu, R.; Zhuang, D.; Sun, S. Materials Cartography: A Forward-Looking Perspective on Materials Representation and Devising Better Maps. *APL Mach. Learn.* **2023**, *1*, No. 020901.
(49) LeCun, Y.; Bengio, Y.; Hinton, G. Deep Learning. *Nature* **2015**, *521*, 436−444.
(50) Oganov, A. R.; Pickard, C. J.; Zhu, Q.; Needs, R. J. Structure Prediction Drives Materials Discovery. *Nat. Rev. Mater.* **2019**, *4*, 331−348.
(51) Yao, Y.; Dong, Q.; Brozena, A.; Luo, J.; Miao, J.; Chi, M.; Wang, C.; Kevrekidis, I. G.; Ren, Z. J.; Greeley, J.; Wang, G.; Anapolsky, A.; Hu, L. High-Entropy Nanoparticles: Synthesis-Structure-Property Relationships and Data-Driven Discovery. *Science* **2022**, *376* (6589), No. eabn3103.
(52) Rangel DaCosta, L.; Sytwu, K.; Groschner, C. K.; Scott, M. C. A Robust Synthetic Data Generation Framework for Machine Learning in High-Resolution Transmission Electron Microscopy (HRTEM). *npj Comput. Mater.* **2024**, *10*, No. 165.
(53) Boselli, L.; Lopez, H.; Zhang, W.; Cai, Q.; Giannone, V. A.; Li, J.; Moura, A.; de Araujo, J. M.; Cookman, J.; Castagnola, V.; Yan, Y.; Dawson, K. A. Classification and Biological Identity of Complex Nano Shapes. *Commun. Mater.* **2020**, *1*, No. 35.

https://doi.org/10.1021/acsnano.4c09312
ACS Nano 2024, 18, 29736−29747